J. Fluid Mech. (2014), *vol.* 756, *pp.* 110–129. © Cambridge University Press 2014
doi:10.1017/jfm.2014.440

Confinement effects in wind-turbine and propeller measurements

Antonio Segalini[1],† **and Pieter Inghels**[1]

[1]Linné FLOW Centre, KTH Mechanics, S-100 44 Stockholm, Sweden

(Received 25 November 2013; revised 1 July 2014; accepted 24 July 2014;
first published online 1 September 2014)

A new model to account for the presence of the test-section wall in wind-turbine or propeller measurements is proposed. The test section, here assumed to be cylindrical, is modelled by means of axisymmetric source panels, while the wind turbine (or the propeller) is modelled with a simplified vortex model (Segalini & Alfredsson, *J. Fluid Mech.*, vol. 725, 2013, pp. 91–116). Combining both models in an iterative scheme allows the simulation of the effect of the test-section wall on the flow field around the rotor. Based on this novel approach, an analysis of the flow modification due to blockage is conducted together with a comparison of actuator-disk theory results. Glauert's concept of equivalent unconfined turbine is reviewed and extended to account for the angular velocity of the rotor. It is shown that Glauert's equivalent free-stream velocity concept is beneficial and can correct most of the systematic error introduced by the presence of the test-section wall, although some discrepancies remain, especially in the power coefficient. The effect of the confinement on the wake structure is also discussed in terms of wake expansion/contraction, pitch of the tip vortices and forces at the rotor.

Key words: vortex dynamics, vortex flows, wakes/jets

1. Introduction

The estimation of the performance of wind turbines and propellers can be done in several ways. A simple way is the use of the blade-element method (Glauert 1935; Burton *et al.* 2001), where the general momentum theory is combined with the blade-element approximation. However, this approach is limited by the number of approximations involved (for instance, it assumes a rotor with an infinite number of blades, usually corrected by means of tip-loss corrections) and by the need of tabulated aerofoil data. An alternative way that is becoming widespread is the use of numerical methods to simulate the flow around the rotor (Vermeer, Sørensen & Crespo 2003). This is usually achieved by discretizing the domain in space and time and it is therefore computationally expensive to perform, especially if a parametric study with many configurations is pursued. Alternatively, in order to evaluate the performance of an existing rotor, or to validate the numerical results, experimental data can be used, coming either from a real turbine/propeller or from a down-scaled one. For real-scale wind-turbine tests (and to a lesser extent propellers) it is necessary to have available

---

† Email address for correspondence: segalini@mech.kth.se

data measured over a long time period to have statistically significant results (this can add up to data spanning up to 1 or 2 years). A more feasible alternative is to evaluate a down-scaled model of the rotor and do the measurements in an enclosed and controlled environment, usually a wind or water tunnel (from now on we will focus only on wind tunnels but the discussion is valid for water tunnels as well). During the design of these devices, the measurement of the rotor performance in a wind tunnel is a crucial process. Once the preliminary design of the blades is done, experiments are performed to assess the actual behaviour of the turbine and to verify whether or not it operates as designed. During the wind-tunnel experiments, several operating regimes can be investigated under different controlled conditions (free-stream velocity, velocity gradient, temperature, turbulence, etc.). These tests are usually performed on a down-scaled model of the designed wind turbine or propeller, but the model is as big as possible to avoid low-Reynolds-number effects that will significantly change the flow near the rotor blades.

The presence of walls in closed test sections does however have an effect on the flow field around the rotor (see for instance Chen & Liou 2011; McTavish, Feszty & Nitzsche 2013). This is mainly due to the fact that the wake behind the rotor is not allowed to expand or contract in a similar way as it would do in unconfined conditions. In particular, the flow characteristics between the wall and the wake will be significantly modified. While in unconfined conditions the flow outside the wake will recover the properties of the incoming free-stream flow, in an enclosed tunnel the flow behind the wind turbine (propeller) is funnelled into an area with a decreasing (increasing) cross-section size. This will accelerate (decelerate) the flow outside the wake compared to the free-stream velocity. Furthermore, the streamtube upstream of the rotor will expand (contract) less than in the unconfined case, implying a larger working mass flow rate and a higher aerodynamic efficiency that might even overcome the Betz limit for wind turbines. These effects are usually referred to as blockage. It is worth mentioning that this problem also concerns numerical simulations as the boundary condition in the surface surrounding the simulated domain is of zero outward velocity (Sørensen & Shen 2002; Troldborg 2008), a condition equivalent to having a wall that is limiting the flow transversal motions.

A detailed review of blockage-correction schemes was reported by Barlow, Rae & Pope (1999), with a brief mention to propeller corrections where only the work of Glauert (1935) was cited. The strategy that was pioneered by Glauert (and later followed by Mikkelsen & Sørensen 2002; Bahaj *et al.* 2007; Garrett & Cummins 2007; Werle 2010, among others) was focused on the actuator-disk modelling of the propeller, assumed to be a porous, inviscid and homogeneous disk. Furthermore, the flow properties (velocity and pressure) in each cross-section of the streamtube containing the working fluid were assumed to be homogeneous, restricting the analysis to rotors with an infinite number of blades. In addition to the flow analysis, Glauert introduced the definition of the 'equivalent free-stream velocity', U'_∞, that will give the same measured thrust force and disk velocity as in an equivalent unconfined case. The correction of the dimensionless thrust and power coefficients can then be done by simply rescaling them with an appropriate power of the ratio between the equivalent and the measured free-stream velocity, $\sigma = U'_\infty/U_\infty$. Glauert obtained an implicit formula for the equivalent free-stream velocity and then he linearized it in the limit of small blockage ($\epsilon = A_d/C \ll 1$, where A_d is the disk area and C is the test-section cross-section). This linearization works well for propellers, but becomes singular for wind turbines as the thrust coefficient approaches unity. Therefore, it is sometimes erroneously stated that the Glauert correction does not work for highly loaded turbines, although it is more appropriate to refer this to the linearization that he proposed. Similar derivations with simpler algebra were also proposed by Mikkelsen & Sørensen (2002), Garrett & Cummins (2007) and Werle (2010). Despite the age and the limitations for the wind-turbine case, the linearized Glauert approach is still the most used method in the community and it is the benchmark for all the other correction schemes.

The analysis of the wake structure becomes more problematic as the confinement introduces a velocity perturbation in the wake evolution. For instance, tip-loss corrections (closely related to the near-wake structure) might be affected by the effect of the confinement, an issue investigated theoretically only by Goodman (1956). As a rule of thumb, it is often assumed that if $\epsilon < 0.1$ no significant confinement effect is present and the wake resembles the equivalent one without confinement (Wilson 1994). The discussion could be further extended to dynamical phenomena like the wake instability and meandering, although they will not be analysed in the present work.

Flow analyses and corrections schemes not based on the actuator-disk approximation are quite rare. Numerical simulations cannot give general results due to the prohibitive number of cases that need to be evaluated to provide a generalized understanding. On the other hand, analytical results like the ones proposed by Okulov & Sørensen (2010) with a prescribed wake structure cannot be applied since it is unknown how the test-section wall modifies the velocity field around the helical filament.

The availability of a new, fast and accurate numerical model to calculate the near-wake structure and the performance of a rotor (Segalini & Alfredsson 2013) provides the opportunity to build a numerical model of a wind turbine or a propeller placed inside the test-section enclosure. With this it is possible to simulate the effect of the test-section walls on the near-wake structure and the rotor performance. The results can be compared with those of an equivalent rotor operating without confinement, providing a relationship between the two experimental results, and an understanding of how much the flow will be affected by the confinement, and this idea is pursued in the present work. Similarly to actuator-disk-based theories, the present model is developed for axially symmetric flows, so that the results are strictly applicable to circular test sections and ducted propellers, for instance. However, it is expected that the model should also describe well blockage effects in rectangular test sections with $\epsilon \ll 1$.

The paper is structured as follows. Section 2 reviews some results obtained by means of the actuator-disk approximation and introduces a new definition of the equivalent unconfined rotor concept. Basic results of the simple actuator-disk approach will be briefly recalled in order to provide useful relationships for the comparison of the model results. Section 3 provides a description of the wind-turbine/propeller vortex model and of the test-section model, together with their respective numerical implementation. A discussion of the confinement effect and of blockage-correction schemes is reported in § 4 followed by § 5 with some concluding remarks.

2. The actuator-disk method

Let us consider the two axisymmetric control volumes depicted in figure 1. Within the actuator-disk approximation, the flow properties are homogeneous in each cross-section of the inner streamtube. The derivation will be here focused on the wind-turbine case, but it is also applicable to propellers, and it is equivalent to the one proposed by Garrett & Cummins (2007) and Werle (2010). The application of mass conservation and momentum balance principles provides the simple relationships

$$A_w U_w = A_d U_d, \quad (C - A_\infty) U_\infty = (C - A_w) U_2, \qquad (2.1a,b)$$

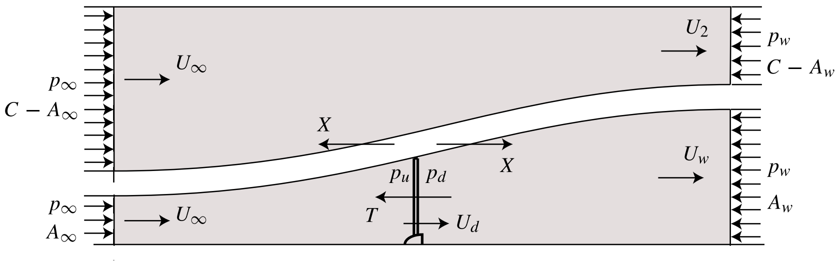

FIGURE 1. Schematic representation of the control volumes used.

and

$$-T + p_\infty A_\infty - p_w A_w + X = \rho A_w U_w^2 - \rho A_\infty U_\infty^2, \tag{2.2}$$

$$p_\infty (C - A_\infty) - p_w (C - A_w) - X = \rho (C - A_w) U_2^2 - \rho (C - A_\infty) U_\infty^2, \tag{2.3}$$

where X is the unknown pressure force applied on the streamtube surface, $T = (p_u - p_d) A_d$ is the thrust force applied by the rotor to the fluid, $A_d = \pi R^2$ is the rotor area and ρ is the fluid density. A_∞ and A_w are the cross-sectional areas of the inlet and outlet sections of the inner control volume, respectively.

By summing (2.2) and (2.3) it is possible to obtain

$$T - (p_\infty - p_w) C = \rho C U_\infty^2 - \rho (C - A_w) U_2^2 - \rho A_w U_w^2. \tag{2.4}$$

By means of Bernoulli's theorem applied upstream and downstream of the rotor and outside the inner streamtube, it is possible to obtain that

$$p_\infty - p_w = \frac{\rho}{2} \left(U_2^2 - U_\infty^2\right) \quad \text{and} \quad p_u - p_d = \frac{\rho}{2} \left(U_2^2 - U_w^2\right). \tag{2.5a,b}$$

Equation (2.4), combined with (2.1), (2.5) and with $T = (p_u - p_d) A_d$, reduces to

$$\epsilon \left(u_2^2 - u_w^2\right) = (u_2 - 1)(u_2 + 2u_w - 1), \tag{2.6}$$

where

$$\epsilon = \frac{A_d}{C}, \quad u_w = \frac{U_w}{U_\infty}, \quad u_2 = \frac{U_2}{U_\infty}. \tag{2.7a–c}$$

Equation (2.6) can be solved in closed form in terms of the wake velocity ratio and blockage parameter as

$$u_2 = \frac{1}{1-\epsilon} \left[1 - u_w + \sqrt{u_w^2 + \epsilon\left(1 - 2u_w - u_w^2\right) + \epsilon^2 u_w^2}\right]. \tag{2.8}$$

Other useful expressions concern the velocity at the disk

$$u_d = \frac{U_d}{U_\infty} = u_w \frac{u_2 + u_w}{u_2 + 2u_w - 1}, \tag{2.9}$$

and the measured thrust coefficient

$$C_T = \frac{2T}{\rho U_\infty^2 A_d} = u_2^2 - u_w^2, \tag{2.10}$$

that can be determined as functions of the wake velocity by means of (2.8). As is usually done in actuator-disk models, the power is determined by considering the work done by the thrust force, $P = TU_d$, so that the power coefficient can be expressed as

$$C_P = \frac{2P}{\rho U_\infty^3 A_d} = u_d \left(u_2^2 - u_w^2\right). \tag{2.11}$$

By means of the actuator-disk approach it is possible to get some insight into the final state of the wake in terms of the wake radius

$$r_{w\infty} = \frac{R_{w\infty}}{R} = \sqrt{\frac{u_d}{u_w}}, \tag{2.12}$$

and pitch

$$p_\infty \approx \frac{u_2 + u_w}{2\lambda r_{w\infty}} = \frac{1}{2\lambda r_{w\infty}\left(1 - \epsilon {r_{w\infty}}^2\right)} \left[1 + \frac{1 - 2\epsilon {r_{w\infty}}^2}{{r_{w\infty}}^2} u_d\right], \tag{2.13}$$

where the approximation is due to the fact that the induced azimuthal velocity is unknown and only the rigid-body rotation of the vortex system (by means of the rotor angular velocity $\varOmega$, or the tip-speed ratio $\lambda = \varOmega R/U_\infty$) is accounted for. This can become a problem in the case of propellers that have high azimuthal velocity and low wake radius.

By using the actuator-disk theory it is possible to approximately describe the flow around an enclosed rotor. However, it is of practical importance to understand how to transfer wind-tunnel measurements (done with confinement) to real turbines (without confinement). Glauert (1935) introduced the definition of an equivalent free-stream velocity, U'_∞, so that a rotor working without nearby walls would have the same thrust and disk velocity (and indeed extracted power) as measured with walls (and with a free-stream velocity U_∞). According to momentum theory, the thrust of an unconfined turbine is

$$T' = 2\rho A_d U'_d \left(U'_\infty - U'_d\right), \tag{2.14}$$

where from now on primes will indicate the equivalent unconfined rotor quantities. Equation (2.14) can be normalized with $\rho U_\infty^2 A_d/2$ giving $C_T = 4u_d\,(\sigma - u_d)$. This expression provides a simple estimate of the equivalent free-stream velocity ratio (Mikkelsen & Sørensen 2002) as

$$\sigma = \frac{U'_\infty}{U_\infty} = u_d + \frac{C_T}{4u_d}. \tag{2.15}$$

In the limit of $\epsilon \rightarrow 0$, (2.8), (2.10) and (2.15) can be linearized, leading to the simple Glauert formula

$$\sigma = 1 + \epsilon \frac{C_T}{4\sqrt{1 - C_T}}. \tag{2.16}$$

As discussed in the introduction, this formula is very useful for propellers (where $C_T < 0$), but becomes singular for wind turbines with $C_T \rightarrow 1$.

At this point a theoretical drawback of actuator-disk theory appears. As discussed by Segalini & Alfredsson (2013), the thrust and disk velocity are related to the free-stream velocity, U_∞, the angular velocity, $\varOmega$, and the strength of the vortex system, here identified by means of the blade circulation, $\varGamma$, while the rotor radius, R, and the number of blades are here supposed to be geometric constants. Any derived quantity, like the disk velocity or the thrust, will be a function of these three parameters (U_∞, $\varOmega$ and $\varGamma$). In Glauert's equivalent free-stream velocity concept there is only the matching between two parameters (T and U_d), with an infinite number of possible configurations that fulfil the constraints. This problem appears in practical situations when correcting the power-coefficient curve versus the tip-speed ratio. In fact, while Glauert's theory suggests that the power coefficient should be scaled with σ^3, the tip-speed ratio leaves some ambiguity: is the equivalent free-stream velocity concept associated with a constant angular velocity, $\varOmega$, or with a constant tip-speed ratio, or with neither of them? Actuator-disk-based approaches cannot give an answer to this question and, to the authors' knowledge, nobody has attempted a description of blockage effects by means of general momentum theory, probably because of the unknown distribution of pressure force applied on each infinitesimal streamtube section (see Glauert 1935). In the present work, the equivalent unconfined turbine is defined as the turbine that will give the same disk velocity, thrust force and tip-speed ratio so that the conditions

$$U_d = U_d', \quad T = T' \quad \text{and} \quad \lambda = \frac{\varOmega R}{U_\infty} = \frac{\varOmega' R}{U_\infty'} = \lambda', \tag{2.17a–c}$$

are fulfilled between the confined and the equivalent unconfined rotor. Other definitions of the equivalent unconfined rotor could be used, for instance by requiring the matching of the rotor angular velocity rather than the tip-speed ratio. This alternative has been investigated by the authors and the results of this analysis were close to the ones obtained for constant λ, although affected by a larger scatter due to the more complicated procedure to determine the equivalent unconfined rotor (see § 4.2 for a discussion about the determination of the equivalent unconfined rotor).

3. Model description

The basic building blocks of the enclosed turbine model are a free-vortex model to replicate the rotor and its wake (Segalini & Alfredsson 2013), together with a panel method (composed of discrete sources) to model the test-section wall. Both models assume a steady-state, incompressible, inviscid and irrotational flow everywhere with the exception of the region occupied by the vortex filaments that compose the rotor wake. Differently from the unconfined case, the radial flow is attenuated by the test-section wall, and thus the wall-normal induced velocity imparted by the rotor at the wall location needs to be cancelled by the distributed sources. As a side effect, the sources induce a certain velocity field throughout the domain that is felt in the rotor wake. This external perturbation velocity has an effect on the wake shape and thus on the velocity induced by the rotor on the test-section wall, so that the source-strength distribution has to be adapted iteratively to the new induced velocity from the rotor. Since the vortex method is an iterative scheme, the complete model of rotor and tunnel will be solved by means of an iterative approach as well.

To account for the turbine rotation, a rotating reference frame is introduced, according to figure 2. In such a reference frame, the x-axis is aligned with the first

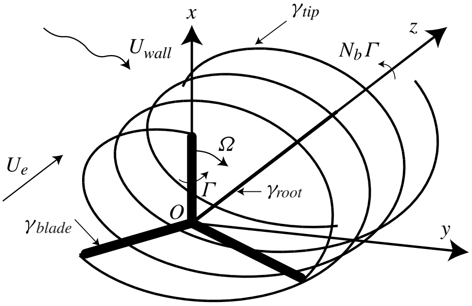

FIGURE 2. Schematic representation of the vortex model and its reference frame.

blade, the z-axis is oriented normal to the rotor plane and the y-axis is chosen normal to both the x- and z-axes. The origin of the reference frame is chosen to be located at the rotor hub. The angular velocity of the rotor is aligned with the z-axis, $\boldsymbol{\Omega} = \Omega^* \boldsymbol{e}_3$ (with $\boldsymbol{e}_3 = [0, 0, 1]$). The unperturbed free-stream velocity is also oriented along the z-axis, so that $\boldsymbol{U}_e = U_e^* \boldsymbol{e}_3$. This unperturbed (also referred to here as external) free-stream velocity is different from the one that could be measured inside the test section (indicated with U_∞^*, consistently with the notation of the previous section) that is affected by the turbine's presence. Consider for instance the unperturbed stream with velocity U_e^* and a frictionless pipe aligned along $\boldsymbol{e}_3$: the velocity inside the pipe (here denoted U_∞^*) will be equal to U_e^* as well. However, if inside the pipe there is a force $T \neq 0$, the velocity inside the pipe will be $U_\infty^* \neq U_e^*$. In general, if $T \geqslant 0$ (namely the force is directed upwind and slowing the flow down), $U_\infty^* \leqslant U_e^*$ and vice versa. U_∞^* can only be determined *a posteriori* by computing the mass flow inside the test section upstream of the rotor (in the present implementation it is evaluated at $z^* = -50R^*$) so that the radial and azimuthal variation of the blockage from the turbine itself can be neglected (Medici *et al.* 2011).

From this section to the end of the paper, all dimensional quantities (indicated with an asterisk superscript) will be scaled with the fluid density, ρ^*, the external free-stream velocity, U_e^*, and the rotor radius, R^*, to obtain the non-dimensional variables

$$\lambda_e = \frac{\Omega^* R^*}{U_e^*}, \quad \Gamma_e = \frac{\Gamma^*}{U_e^* R^*}, \quad \delta = \frac{\delta^*}{R^*}, \quad R_t = \frac{R_t^*}{R^*}, \quad \boldsymbol{x} = \frac{\boldsymbol{x}^*}{R^*}, \tag{3.1a–e}$$

where Γ^*, δ^* and R_t^* are the circulation along the blade, the constant radius of the vortex tube along the blade (and the tip vortex) and the test-section radius, respectively; $\boldsymbol{x} = [x, y, z]$ is the dimensionless position vector. For practical use, the model is formulated in terms of U_e^* so that quantities normalized with this velocity scale will be marked with a subscript e, otherwise quantities will be reported using U_∞^* as velocity scale. Consistently with the previous section, primed quantities will be generally associated with unconfined conditions including the equivalent unconfined rotors.

3.1. *Rotor vortex model*

The vortex model used here is based on discrete vortex filaments to simulate the rotor wake, originally proposed by Joukowsky (1912) and extended by Segalini & Alfredsson (2013), schematically depicted in figure 2. The model assumes a constant circulation along the blade implying that the modelled turbine operates approximately at maximum efficiency for a given set of operating conditions (Okulov & Sørensen 2010). The main goal of the model is to calculate the tip-vortex path iteratively, allowing for the wake expansion or contraction. Once the tip-vortex path is known, the velocity induced by the vortex system in the domain can be calculated by means of the Biot–Savart law (Batchelor 1967).

The blades are modelled with N_b vortex lines with constant circulation, Γ^*. The vorticity is assumed to be oriented parallel to the vortex-line axis and it is distributed uniformly within a radius δ^* from the axis. The value of δ^* is constant along each filament, so that viscous diffusion and vortex stretching are neglected. The root-vortex path is assumed to be straight and described by $\boldsymbol{\gamma}_{root} = z\boldsymbol{e}_3$, while the tip-vortex path is assumed to be helix-like shaped with a variable radius and pitch. For the first blade, this vortex path can be described by

$$\boldsymbol{\gamma}_{tip} = r_w(z)\boldsymbol{\Psi} + z\boldsymbol{e}_3, \tag{3.2}$$

with the orthogonal unitary vectors

$$\boldsymbol{\Psi} = [\cos\phi_w, \sin\phi_w, 0], \qquad \tilde{\boldsymbol{\Psi}} = [-\sin\phi_w, \cos\phi_w, 0], \tag{3.3a,b}$$

where $\phi_w = \phi_w(z)$. The description of the three-dimensional tip-vortex filament is therefore reduced to knowledge of two scalar functions, representing the local wake radius, $r_w(z)$, and filament phase, $\phi_w(z)$, respectively, that, together with (3.2) and (3.3), allow the tip-vortex path description in the rotating reference frame. By means of flow symmetry, the tip-vortex paths associated with the other blades have the same radial function, $r_w(z)$, while the phase function, $\phi_w(z)$, is shifted for each blade by $\Delta\phi = 2\pi/N_b$.

Each blade is modelled as a straight vortex line, described mathematically by $\boldsymbol{\gamma}_{blade,i} = r[\,\cos\alpha_i,\ \sin\alpha_i, 0\,]$ where $\alpha_i = 2\pi\,(i-1)\,/N_b$ is the azimuthal position of the ith blade and $r = (x^2+y^2)^{1/2} \leqslant 1$ is the normalized radial location at the rotor disk.

The tip-vortex radial function, $r_w(z)$, and angular function, $\phi_w(z)$, can be determined by means of the Helmholtz theorems, by considering that the tip-vortex filament must be a flow streamline. The velocity vector at each point of the tip vortex can be computed by adding three contributions, namely the free-stream contribution, $\boldsymbol{e}_3$, the velocity induced by the test-section wall presence, $\boldsymbol{u}_{wall,e}$, and the velocity induced by the vortex system itself, $\boldsymbol{u}_{f,e}$. In a rotating reference frame, the streamlines are steady and the following kinematic equation holds:

$$\left[\boldsymbol{u}_{f,e}(\boldsymbol{\gamma}_{tip}) + \boldsymbol{e}_3 + \boldsymbol{u}_{wall,e}(\boldsymbol{\gamma}_{tip}) - \lambda_e\boldsymbol{e}_3 \times \boldsymbol{\gamma}_{tip}\right] \times \frac{\mathrm{d}\boldsymbol{\gamma}_{tip}}{\mathrm{d}z} = 0, \tag{3.4}$$

where the first three terms indicate the normalized velocity contributions discussed above and the fourth term indicates the change to a rotating reference frame. Given that

$$\frac{\mathrm{d}\boldsymbol{\gamma}_{tip}}{\mathrm{d}z} = \frac{\mathrm{d}r_w}{\mathrm{d}z}\boldsymbol{\Psi} + r_w\frac{\mathrm{d}\phi_w}{\mathrm{d}z}\tilde{\boldsymbol{\Psi}} + \boldsymbol{e}_3, \tag{3.5}$$

equation (3.4) can be rearranged to obtain the following two ordinary differential equations for $r_w(z)$ and $\phi_w(z)$:

$$\frac{\mathrm{d}r_w}{\mathrm{d}z} = -\frac{[(\boldsymbol{u}_{f,e} + \boldsymbol{u}_{wall,e}) \times \boldsymbol{e}_3]\boldsymbol{\cdot}\tilde{\boldsymbol{\Psi}}}{1 + [(\boldsymbol{u}_{f,e} + \boldsymbol{u}_{wall,e}) \times \boldsymbol{\Psi}]\boldsymbol{\cdot}\tilde{\boldsymbol{\Psi}}}, \tag{3.6}$$

$$r_w\frac{\mathrm{d}\phi_w}{\mathrm{d}z} = \frac{\lambda_e r_w - [(\boldsymbol{u}_{f,e} + \boldsymbol{u}_{wall,e}) \times \boldsymbol{e}_3]\boldsymbol{\cdot}\boldsymbol{\Psi}}{[(\boldsymbol{u}_{f,e} + \boldsymbol{u}_{wall,e}) \times \tilde{\boldsymbol{\Psi}}]\boldsymbol{\cdot}\boldsymbol{\Psi} - 1}. \tag{3.7}$$

Since solving this set of equations requires knowledge of $\boldsymbol{\gamma}_{tip}$, an iterative scheme is needed. Initially the tip vortex is assumed to be a helix with constant radius and linear phase. The induced velocity is therefore computed and, by means of (3.6) and (3.7), two updated distributions of $r_w(z)$ and $\phi_w(z)$ are determined. The process is iterated several times until the changes in the path geometry fall below a certain threshold.

To compute the induced velocity due to the presence of the vortex lines, the Biot–Savart law is applied. As discussed by Segalini & Alfredsson (2013), the velocity induced by the vortex system must be computed at all points of the tip vortex. For a generic point of $\boldsymbol{\gamma}_{tip}$, the line-vortex approximation of the Biot–Savart law can be used if the filament is far enough from the point of interest. Otherwise, finite core effects must be accounted for, especially concerning the self-induced velocity calculation (see for instance Callegari & Ting 1978; Fukumoto & Miyazaki 1991; Ricca 1994; Kuibin & Okulov 1998; Leishman 2000).

The thrust and power coefficients, here defined as

$$C_{T,e} = \frac{2T^*}{\rho^* \left(U_e^*\right)^2 A_d^*}, \quad C_{P,e} = \frac{2P^*}{\rho^* \left(U_e^*\right)^3 A_d^*}, \tag{3.8a,b}$$

can be calculated by the integration over the normalized blade length, r, of the following expressions:

$$C_{T,e} = \frac{2}{\pi} N_b \Gamma_e \int_0^1 \left[\left(\boldsymbol{u}_{f,e}(\boldsymbol{\gamma}_{blade}) + \boldsymbol{e}_3 + \boldsymbol{u}_{wall,e}(\boldsymbol{\gamma}_{blade}) - \lambda_e r \boldsymbol{e}_2\right) \times \boldsymbol{e}_1\right] \boldsymbol{\cdot} \boldsymbol{e}_3 \, \mathrm{d}r, \tag{3.9}$$

$$C_{P,e} = \frac{2}{\pi} \lambda_e N_b \Gamma_e \int_0^1 \left[\left(\boldsymbol{u}_{f,e}(\boldsymbol{\gamma}_{blade}) + \boldsymbol{e}_3 + \boldsymbol{u}_{wall,e}(\boldsymbol{\gamma}_{blade}) - \lambda_e r \boldsymbol{e}_2\right) \times \boldsymbol{e}_1\right] \boldsymbol{\cdot} \boldsymbol{e}_2 r \, \mathrm{d}r. \tag{3.10}$$

3.2. *Test-section model*

Since the vortex model determines the steady-state condition, the test-section wall must also impose a boundary condition that is independent of the rotation of the turbine. This restricts the analysis to cylindrical test sections with the cylinder axis coinciding with the rotor axis. With this particular shape, the use of a rotating reference frame will have no implications with respect to the tunnel presence as the condition imposed by the wall concerns only the radial velocity which is unaffected by the rotation. This particular scenario also approximates non-circular test sections if $\epsilon \ll 1$ as well as ducted propellers.

Initially, the wall was modelled with quadrilateral source panels (Katz & Plotkin 1991) located at the tunnel wall, but this methodology was soon abandoned. When the variation of the radial velocity at the wall location is small (compared to its average value), the induced radial velocity can be assumed to be axisymmetric, implying that the circumferential distribution of the source strength can be assumed to be axisymmetric as well. When this is the case, cylinder-shaped sources of constant strength can be used to enforce the wall boundary condition, significantly reducing the number of unknowns to be determined.

Figure 3 shows the azimuthal average of the radial velocity (and its azimuthal peak-to-peak variation) for a one-bladed and a two-bladed wind turbine operating in unconfined conditions, both evaluated at a given z position and at two fixed radial distances from the wind-turbine axis of $2R^*$ and $3R^*$ (no effect of the test-section wall presence is taken into account here). As visible from the figure, both the single-bladed and the two-bladed rotors have a small peak-to-peak variation at $3R^*$,

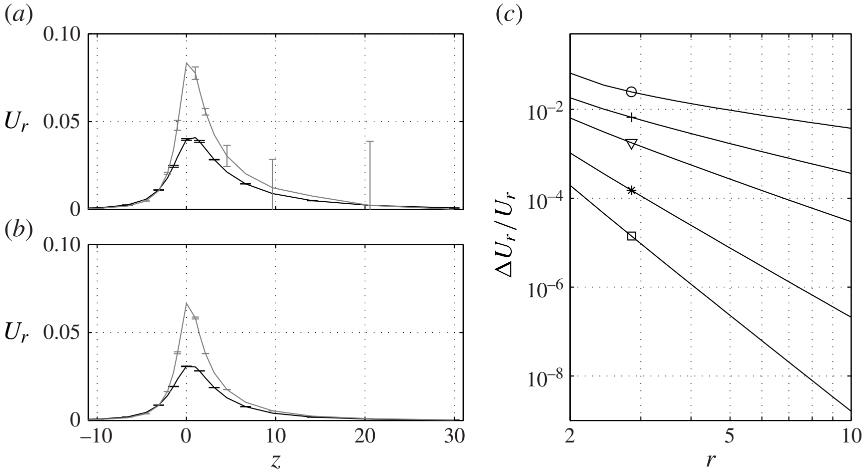

FIGURE 3. Axial distribution of the azimuthally averaged radial velocity, U_r, induced by an unconfined wind turbine operating at $\lambda' = 5$ and $\lambda' N_b \Gamma' = 8\pi/9$ with (*a*) $N_b = 1$ and (*b*) $N_b = 2$ at a radial distance of $2R^*$ (grey lines) and $3R^*$ (black lines). The error bars indicate the maximum–minimum variation of U_r (denoted by ΔU_r) evaluated at several azimuthal positions. (*c*) Radial distribution of $\Delta U_r/U_r$ at $z = 0$ for $\circ$, $N_b = 1$; $+$, $N_b = 2$; $\triangledown$, $N_b = 3$; $*$, $N_b = 5$; and $\square$, $N_b = 7$.

but at $2R^*$ the azimuthal variation is non-negligible in the single-bladed case. The same trend is observed at a certain radial distance below $2R^*$ for the two-bladed case also, and similarly for cases with a higher number of blades. Indeed, the radial velocity distribution can be generally assumed to be axisymmetric for radial distances greater than $3R^*$, while for $N_b \geqslant 2$ this bound is lowered to $2R^*$. At the rotor axial location, the variation is usually the greatest and it decays quickly as the radial location moves further away from the rotor axis. The figure demonstrates the validity of the axisymmetric approximation for the cylindrical test-section wall with $N_b \geqslant 1$ when the test-section radius is larger than a certain threshold (always smaller than $3R^*$) that strongly depends on the number of blades.

Let us now consider the velocity induced by an axisymmetric source cylinder on a generic point $P \equiv [x_0, y_0, z_0]$. The cylinder axis is assumed to lie along the z-axis and the cylinder mid-axial point is assumed to be the origin of the local reference frame used. The radius of the cylinder, length and source strength will be denoted by R_r, $2L_r$ and χ, respectively. By means of symmetry considerations, the velocity induced by the cylinder at point P can only be axially and radially directed depending on the axial and radial position of P (the radial position will be indicated by $r_0 = \left(x_0^2 + y_0^2\right)^{1/2}$). A rotation of the reference frame can be done so that P lies in the xz-plane with coordinates $P = (r_0, 0, z_0)$. The potential of the source cylinder is

$$\Phi\,(r_0, z_0) = -\frac{\chi R_r}{4\pi} \int_0^{2\pi} \mathrm{d}\theta \int_{-L_r}^{L_r} \frac{\mathrm{d}\eta}{\sqrt{(r_0 - R_r\cos\theta)^2 + (z_0 - \eta)^2 + (R_r \sin\theta)^2}}, \tag{3.11}$$

which can be integrated to give

$$\Phi = -\frac{\chi R_r}{4\pi} \int_0^{2\pi} \left[\sinh^{-1}\left(\frac{L_r - z_0}{G}\right) + \sinh^{-1}\left(\frac{L_r + z_0}{G}\right)\right] \mathrm{d}\theta, \tag{3.12}$$

with $G^2 = R_r^2 + r_0^2 - 2R_r r_0 \cos\theta$.

The axial and radial velocity can be calculated after some algebra as

$$u_z = \frac{\partial \Phi}{\partial z_0} = \frac{\chi R_r}{\pi}[F_1 - F_2], \tag{3.13}$$

$$u_r = \frac{\partial \Phi}{\partial r_0} = \frac{\chi R_r}{2\pi r_0}\left[(L_r - z_0)F_1 + (L_r + z_0)F_2 + \frac{r_0 - R_r}{r_0 + R_r}(F_3 + F_4)\right], \tag{3.14}$$

with

$$F_1 = \frac{1}{\sqrt{(R_r + r_0)^2 + (L_r - z_0)^2}} K\left[\frac{4R_r r_0}{(R_r + r_0)^2 + (L_r - z_0)^2}\right], \tag{3.15}$$

$$F_2 = \frac{1}{\sqrt{(R_r + r_0)^2 + (L_r + z_0)^2}} K\left[\frac{4R_r r_0}{(R_r + r_0)^2 + (L_r + z_0)^2}\right], \tag{3.16}$$

$$F_3 = \frac{L_r - z_0}{\sqrt{(R_r + r_0)^2 + (L_r - z_0)^2}} \Pi\left[\frac{4R_r r_0}{(R_r + r_0)^2}, \frac{4R_r r_0}{(R_r + r_0)^2 + (L_r - z_0)^2}\right], \tag{3.17}$$

$$F_4 = \frac{L_r + z_0}{\sqrt{(R_r + r_0)^2 + (L_r + z_0)^2}} \Pi\left[\frac{4R_r r_0}{(R_r + r_0)^2}, \frac{4R_r r_0}{(R_r + r_0)^2 + (L_r + z_0)^2}\right], \tag{3.18}$$

where $K(\alpha)$ and $\Pi(\alpha, \beta)$ are the complete elliptic integrals of the first and third kind, respectively defined as

$$K(\alpha) = \int_0^{\pi/2} \frac{1}{\sqrt{1 - \alpha \sin^2\theta}} \mathrm{d}\theta, \quad \Pi(\alpha, \beta) = \int_0^{\pi/2} \frac{1}{1 - \alpha \sin^2\theta} \frac{1}{\sqrt{1 - \beta \sin^2\theta}} \mathrm{d}\theta. \tag{3.19a,b}$$

The resulting velocity field for a positive unitary source cylinder is shown in figure 4. As expected, close to the cylinder the velocity vector is radially directed and large in magnitude while it becomes more axially directed away from it, with a stagnation point at the origin. Furthermore, the velocity perturbation vanishes at large distances from the cylinder surface, although the surface integral of the outward flow must remain constant, imposing a decay of the perturbation velocity as the square of the distance. It should be noted now that the region close to the cylinder surface deserves some special treatment as the elliptic integrals become singular as $r_0 \rightarrow R_r$ and $z_0 = O(L_r)$. This is problematic if the source cylinder coincides with the test-section wall of the present model. This issue has been circumvented by setting the source-cylinder radius to be $R_r > R_t$ (in the present implementation $R_r = 1.1R_t$) so that the test-section control point is located away from the source surface and the singularity is avoided.

The cylindrical test-section wall has been discretized into n segments and the associated source-cylinder position determined: the source cylinders are placed at the same axial locations as the discretized test-section wall elements but at a larger radial distance to avoid singular behaviour. To determine the strength of the n distributed sources, χ_i, n control points located at the test-section wall are needed. At these control points the condition of zero normal velocity is enforced. For each control point P, the boundary condition can be written as

$$\sum_{i=1}^{n} \chi_i \boldsymbol{V}_i(P) \cdot \boldsymbol{e}_r = -\boldsymbol{V}_{ext}(P) \cdot \boldsymbol{e}_r, \tag{3.20}$$

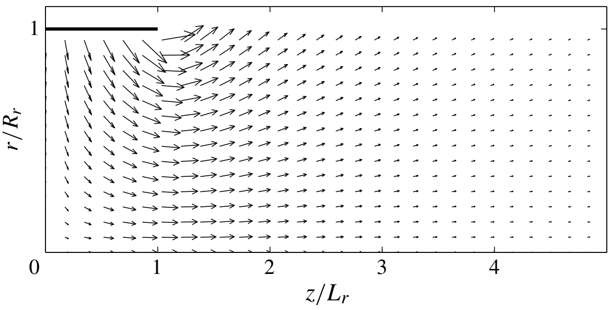

FIGURE 4. Vector field of a unitary cylinder-shaped panel with $R_r = L_r = 1$.

where n is the total number of sources, χ_i the source strength of the ith-panel, $\boldsymbol{V}_i(P)$ the velocity component induced by the ith-source (with unitary source strength) at point P and $\boldsymbol{V}_{ext}(P)$ is the external induced velocity at point P due to the turbine vortex system. The unit vector $\boldsymbol{e}_r$ is radially directed to indicate that the condition must be applied only in the radial direction for this particular test-section geometry.

In order to have a smooth transition from a fine discretization (needed in the proximity of the rotor where the radial velocity is the largest) to a coarse discretization (to be used at large distances from the rotor plane), a linear axial refinement of the cylinder length, $2L_r$, is introduced. In this work, the cylindrical test section extends upstream and downstream of the turbine for 100 rotor radii ($z \in [-100, 100]$) with 196 cylinder elements that are $0.05R^*$ long close to the rotor ($z = 0$) becoming $2R^*$ long at $z = \pm 100$.

4. Results

4.1. *Effect of confinement*

The effect of the test-section confinement radius, R_t, is analysed in the present section by comparing several confined wind turbines equivalent to the same unconfined one (the case of propellers is discussed in the next section from a general point of view). As discussed in § 2, the equivalent unconfined turbine has the same disk velocity, thrust force and tip-speed ratio as the confined one. Figure 5 shows a comparison of the wake structure observed in unconfined and confined conditions ($R_t = 2$, namely $\epsilon = R_t^{-2} = 0.25$). The wake expansion is visibly reduced by the presence of the wall and it achieves its final size much earlier than the unconfined turbine. On the other hand, the flow outside the wake is accelerated and, consequently, the pitch of the tip vortices is significantly increased, so that the tip vortices travel a longer distance during one revolution.

The systematic trend in wake radius and pitch (here defined as $p^{-1} = r_w\,(\mathrm{d}\phi_w/\mathrm{d}z)$) is further investigated in figure 6 for different test-section radii. It is clearly visible that the change in the wake structure is monotonic in both parameters. While the wake radius decreases, the pitch increases compared to the equivalent unconfined case. Consistently with the discussion above, by increasing the blockage the wake is also achieving its asymptotic state more quickly. The comparison of the model outcome with the actuator-disk results is reasonably good, demonstrating that the existing actuator-disk theory is able to provide an estimation of the wake structure reasonably close to the one obtained with the present model.

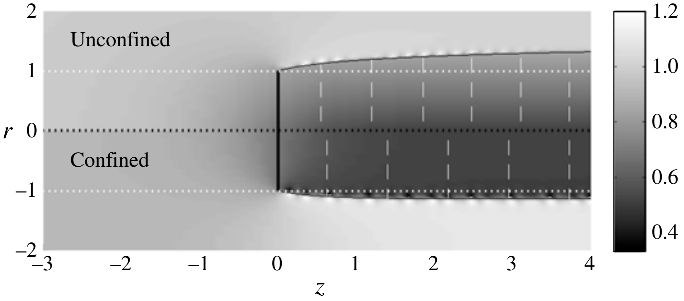

FIGURE 5. Axial velocity field around a three-bladed wind turbine operating at $\lambda'=7$ and $\lambda' N_b \Gamma' = 8\pi/9$ for the unconfined and its equivalent confined case (with $\epsilon = 0.25$). The observation plane is located at the azimuthal position between two consecutive blades ($\theta = \pi/3$). The thin solid black line indicates the radial position of the wake edge while the vertical dashed white lines indicate the axial position of the same tip vortex intersecting the plane.

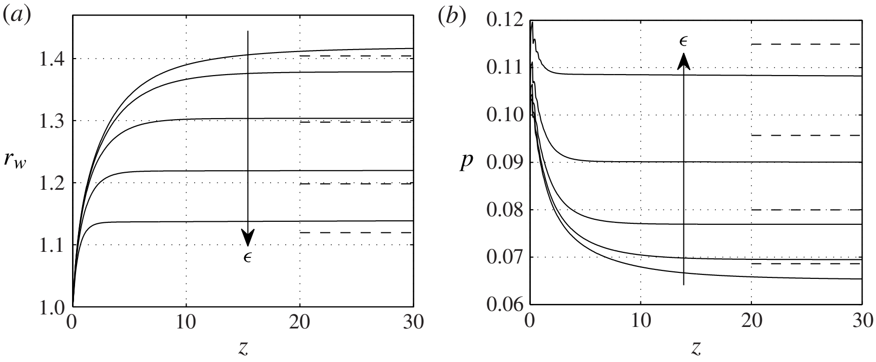

FIGURE 6. Effect of the test-section radius on (*a*) the wake radius and (*b*) pitch for a three-bladed wind turbine operating at $\lambda' = 7$ and $\lambda' N_b \Gamma' = 8\pi/9$. The arrows indicate decreasing test-section radius for the confined equivalent cases (ϵ = 0, 0.01, 0.04, 0.11, 0.25). The dashed lines indicate the associated actuator-disk results from (2.12) and (2.13) obtained by matching the measured thrust coefficient for the cases with these ϵ values.

Force distributions are also expected to be affected by the confinement: this is visible in figure 7 where the normal (to the disk) and tangential (to the disk) force coefficients (C_n and C_t, respectively) are shown. Such coefficients are calculated by normalizing the aerodynamic infinitesimal forces (applied to an annular section of the rotor) by $\rho^*(U^*_\infty)^2 A^*_d/2$ so that the thrust coefficient infinitesimal contribution is given by $\mathrm{d}C_T = N_b C_n \mathrm{d}r$ for instance. Both forces are enhanced for increasing blockage, as a consequence of the increased mass flow through the rotor, and this is something that should be considered during wind-tunnel tests with force or pressure measurements along the blades.

A quantitative assessment of the blockage effect is given in table 1 where the various velocity scales and integral parameters are reported for confined turbines equivalent to the optimal unconfined turbine. It is illustrative to consider first U_∞/U_e, namely the ratio between the free-stream velocity inside the tunnel and the velocity

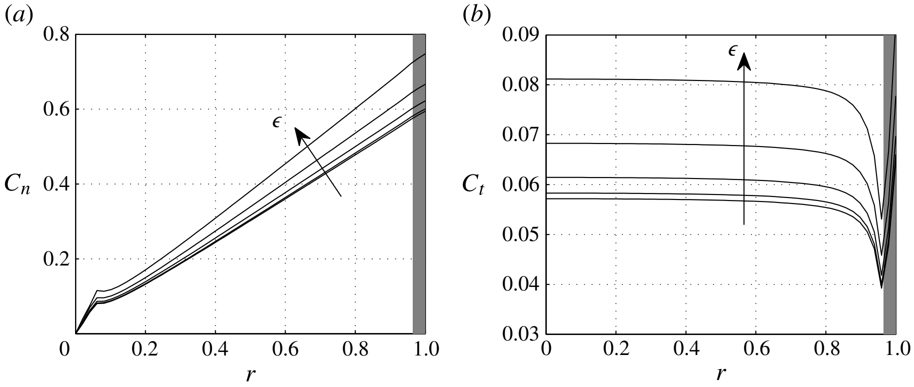

FIGURE 7. Effect of the test-section radius on (*a*) the normal and (*b*) tangential force coefficients for a three-bladed wind turbine operating at $\lambda' = 7$ and $\lambda' N_b \Gamma' = 8\pi/9$. The arrows indicate decreasing test-section radius for the confined equivalent cases ($\epsilon = 0, 0.01, 0.04, 0.11, 0.25$). The shaded area indicates the region affected by core-size effects of the tip vortices.

ϵ	U_∞/U_e	U_d/U_∞	U_w/U_∞	U_2/U_∞	σ	$r_{w\infty}$	C_T	C_P
0	1.000	0.665	0.328	1.000	1.000	1.412	0.916	0.574
0.01	0.994	0.668	0.353	1.012	1.005	1.379	0.926	0.586
0.02	0.989	0.672	0.368	1.024	1.012	1.348	0.938	0.597
0.04	0.978	0.680	0.392	1.044	1.024	1.304	0.960	0.617
0.11	0.950	0.706	0.467	1.104	1.061	1.220	1.031	0.684
0.25	0.908	0.749	0.567	1.201	1.125	1.139	1.160	0.813

TABLE 1. Effect of confinement for an unconfined three-bladed wind turbine with $\lambda' = 7$ and $\lambda' N_b \Gamma' = 8\pi/9$ and the equivalent confined ones.

outside: their discrepancy is related to the force applied by the rotor to the flow and it increases as ϵ increases. As $U'_\infty = \sigma U_\infty \approx U_e$, a simple physical interpretation of the equivalent free-stream velocity can be proposed as the velocity present outside the test-section enclosure, so that the measured free-stream velocity, U_∞, results from the combination of U_e with the induced velocity imparted by the rotor and the cylindrical wall. The approximation is good for lightly loaded rotors and small ϵ values, becoming increasingly inaccurate as C_T and ϵ increase.

Both the disk and wake velocity increase for increasing blockage parameter due to the flow acceleration inside the tunnel. Furthermore, the tunnel attenuates transversal motions (as indicated by the wake radius at $z \to +\infty$, $r_{w\infty}$) and consequently the aerodynamic efficiency is artificially higher due to the test-section wall presence. This is particularly visible in the thrust and power coefficients, where the latter has already exceeded the Betz limit for $\epsilon > 0.02$. It is clear from the table that a highly loaded rotor shows visible blockage effects even for small ϵ. Consequently it can be stated that the area ratio ϵ alone is not sufficient to determine the blockage effect and at least the thrust coefficient should also be accounted, as is clear in the linearized Glauert formula (2.16). In fact, the actual blockage-correction methods use both ϵ and C_T to correct wind-tunnel measurements, providing a first-order correction.

4.2. *Blockage effects*

To assess the effect of the confinement on both the wake structure and rotor performance, more than 2500 configurations were tested for different values of N_b, λ_e, Γ_e and ϵ (note that before the simulation the ratio U_∞/U_e is unknown so only the external free-stream velocity is initially used to scale the data). For all cases, the vortex-core radius, δ, was determined from N_b, Γ_e and λ_e from the roller-bearing analogy of Okulov & Sørensen (2010). Consequently, only four parameters determined the rotor configuration and its blockage: in each case, a set of $(\lambda_e, N_b, \Gamma_e, \epsilon)$ was investigated. By collecting a large number of cases, a detailed map in the parameter space was determined, allowing the identification of the blockage effect and its sensitivity to the loading condition.

An important aspect of interest for wind-tunnel measurements is the equivalent free-stream velocity, U'_∞, or its ratio with the measured free-stream velocity, $\sigma = U'_\infty/U_\infty$. Since $\lambda = \Omega^* R^*/U^*_\infty$ is matched and the equivalent turbine has the same number of blades, only the circulation of the equivalent unconfined turbine, Γ', and σ are unknown. These have been obtained by mapping the functions $U'_d/U'_\infty = f_1(\lambda', N_b, \Gamma')$ and $C'_T = f_2(\lambda', N_b, \Gamma')$ (obtained from the unconfined simulations) and by solving the system of equations

$$\left.\begin{aligned} U_d/U_\infty &= \sigma f_1\left(\lambda, N_b, \Gamma'\right) \\ C_T &= \sigma^2 f_2\left(\lambda, N_b, \Gamma'\right). \end{aligned}\right\} \tag{4.1}$$

Given the tip-speed ratio, $\lambda = \lambda_e U_e/U_\infty$, the disk velocity, U_d/U_∞, and the thrust coefficient, $C_T = C_{Te} U_e^2/U_\infty^2$, of the confined turbine, the system (4.1) was solved to determine σ and Γ' and the equivalent unconfined rotor was determined. The accuracy of the solution of the nonlinear system can be assessed by means of the ratio $U'_d/U_d \approx T'/T \approx 1.0000 \pm 0.0015$ where the reported uncertainty is the 95 % confidence interval and it is due to the numerical approximation involved in obtaining f_1 and f_2 (as they are known at discrete points) and in the solution of the nonlinear system (4.1).

Figure 8 shows a comparison between the equivalent free-stream velocity measured with the present model and the two estimations provided by (2.15) and (2.16) for two different ϵ values. The two analytical expressions almost overlap in the propeller regime while they diverge in the wind-turbine regime as C_T increases. The equivalent free-stream velocity estimated by the present model agrees reasonably well with (2.15) although it should be noted that, as ϵ decreases, some scatter is observed (particularly in the propeller configurations) perhaps due to the secondary effect of different tip-speed ratios and number of blades. Overall, it should be noted that the wind-turbine cases follow the actuator-disk result (2.15), albeit on the lower side, implying that σ is overestimated by the actuator-disk approximation.

Once σ has been determined, the corrected thrust and power coefficients (namely the corresponding equivalent unconfined coefficients) can be determined according to the expressions $C'_T = \sigma^{-2} C_T$ and $C'_P \approx \sigma^{-3} C_P$: while the first is an identity, as the thrust force between equivalent turbines is matched and σ is actually determined from the system (4.1), the second is an approximation as it assumes that the extracted power is equal to the work of the thrust force alone, without any exchange of angular momentum between the rotor and the flow. Figure 9 shows the effect of such a correction on the performance coefficients: while the uncorrected data indicate a significant positive systematic error with respect to the equivalent rotor coefficients, the use of the equivalent free-stream velocity is beneficial and compensates for most of the blockage effect also for the wind-turbine case. Another interesting practical aspect of the correction scheme is shown in figure 10 where the ratio between the

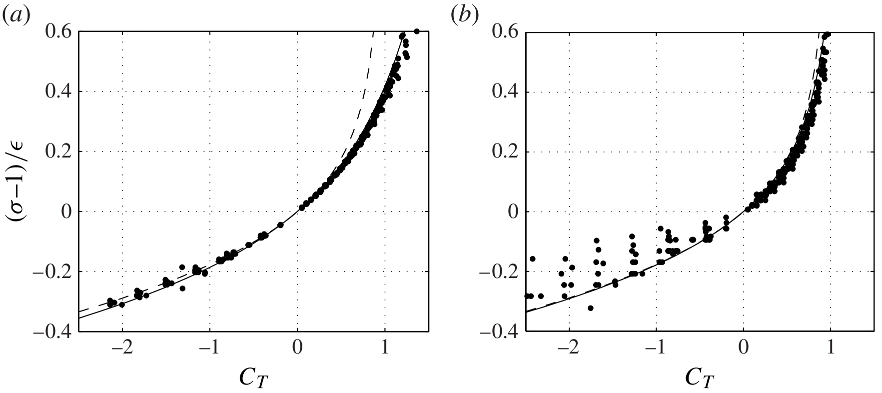

FIGURE 8. Normalized equivalent free-stream velocity ratio measured with the present model (symbols) for (*a*) $\epsilon = 0.25$ and (*b*) $\epsilon = 0.04$. The solid line is (2.15) while the dashed line is the linearized solution proposed by Glauert (2.16).

corrected and equivalent thrust and power coefficient is plotted against C_T, with σ estimated by solving the system (4.1) or by means of (2.15). The actuator-disk expression is able to correct the performance parameters within ±3 % with a larger scatter than the σ estimated in the present model. It is also clear that the discrepancy increases for increasing rotor loading.

The wake structure, and its modification due to blockage, is investigated in figure 11 in terms of wake radius downstream of the rotor, $r_{w\infty}$, and scaled pitch, $\lambda r_{w\infty} p_\infty$. As discussed in the previous section, the wake radius is greatly affected by the presence of the test-section wall. Depending on the magnitude and sign of the circulation, the wake expands/contracts more but this is damped compared to the equivalent unconfined case. The actuator-disk approximation is able to determine this trend for lightly loaded conditions, but the discrepancies increase as C_T increases or, equivalently, as the product $\lambda N_b \Gamma$ increases. Even at the smallest $\epsilon = 0.01$, usually considered as a condition not affected by blockage, the highly loaded turbine wake radius is noticeably reduced.

The discussion about the pitch is not trivial as it is not obvious why the test-section wall should affect it, especially when the tip-speed ratio and the disk velocity are matched. The actuator-disk theory is quite limited since (2.13) does not account for the azimuthal velocity of the tip vortices, which can become a significant contribution for high blockage or in propeller configurations, as in both cases the wake radius is small and the azimuthal velocity imparted by the root vortex is significant. However, it is found that the simple relationship $\lambda r_{w\infty} p_\infty \approx \lambda' r'_{w\infty} p'_\infty \sigma^2$ is already able to provide a quick estimation of the scaled pitch of the equivalent unconfined turbine within ±2 % at $\epsilon = 0.11$.

5. Conclusions

In the present paper the effect of confinement in wind-tunnel measurements of wind turbines and propellers is discussed by means of a simplified numerical model. The rotor presence is simulated by means of the free-vortex system proposed by Segalini & Alfredsson (2013), where the wake is free to modify its shape according to the combination of the free-stream velocity, the perturbation velocity

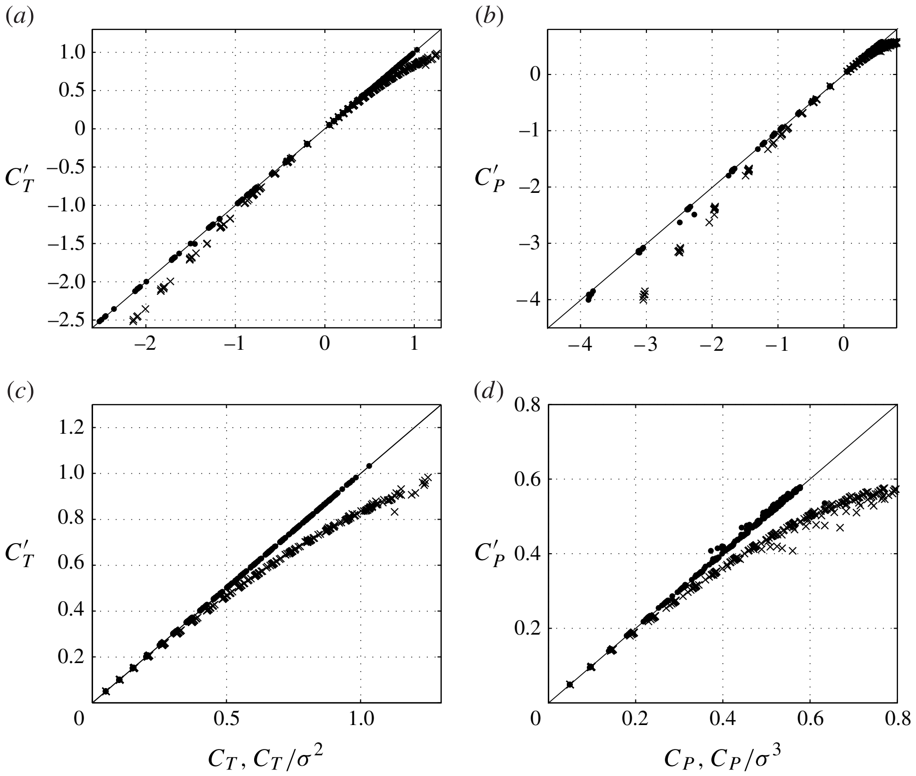

FIGURE 9. Measured (×) and corrected (●) (*a*) thrust and (*b*) power coefficients against the equivalent unconfined value for $\epsilon = 0.25$. (*c*, *d*) The same as in (*a*) and (*b*) but for the wind-turbine cases only.

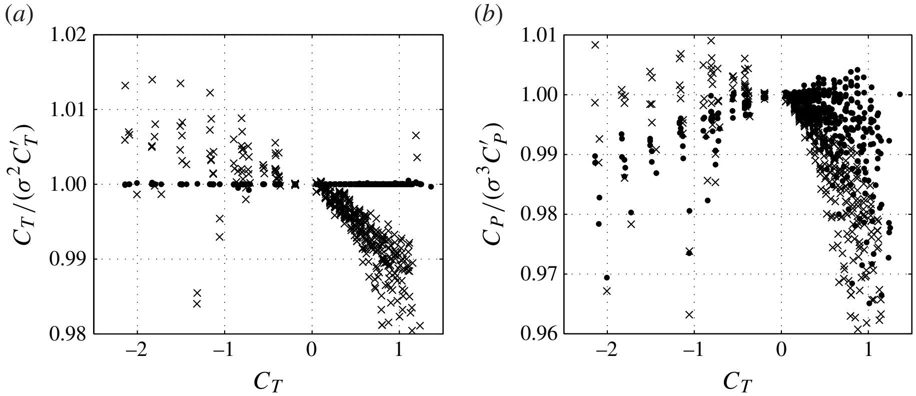

FIGURE 10. Ratio between the corrected (*a*) thrust and (*b*) power coefficients and the equivalent unconfined ones: (●), measured σ; ×, σ estimated from (2.15).

due to the wall presence and the velocity field of the vortex system. The rotor is placed on the axis of a cylindrical test section that cancels the wall-normal velocity component at the wall location. For test-section radius larger than a certain threshold

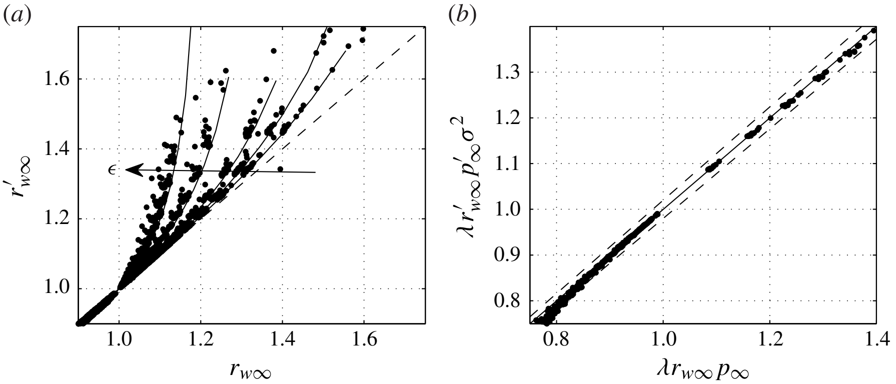

FIGURE 11. (*a*) Comparison of the wake radius of the enclosed rotor against the wake radius of the equivalent unconfined turbine for $N_b \geqslant 2$. The solid lines are the estimation provided by actuator-disk theory for $\epsilon = 0, 0.01, 0.04, 0.11, 0.25$. (*b*) Comparison of the scaled pitch for $\epsilon = 0.25$. The dashed lines indicate an error of ±2 %.

(approximately $R_t > 3$ for $N_b = 1$ and $R_t > 2$ for $N_b \geqslant 2$), the radial velocity is approximately axisymmetric and this approximation improves for larger distances from the axis. As a consequence of this axial-symmetry approximation, the cylindrical test-section wall was replaced by source cylinders that generate a velocity field able to cancel the radial velocity induced by the rotor. The strength of each cylinder is constant over its surface, ensuring the axial symmetry and allowing an analytical solution in terms of complete elliptic integrals. The unknown source-strength distribution is therefore determined by forcing zero radial velocity at several control points (located at the test-section wall and at least one per cylinder) iteratively. The rotor wake adjusts to the wall-velocity perturbation, modifying in turn the induced velocity at the wall and the source strength. The process is iterated until convergence is reached in both the tip-vortex shape and the source-strength distribution.

The results have been first compared to the traditional actuator-disk approximation and subsequently to the established concept of equivalent unconfined rotor. It has been noted that such a concept is incomplete as it leaves out any information about the number of blades (assumed to be infinity) and the angular velocity of the turbine (no angular momentum transfer takes place between the flow and the rotor in actuator-disk theory). Therefore, a new definition of equivalent unconfined rotor is introduced as that with the same number of blades, disk velocity, thrust force and tip-speed ratio as the confined one. Several tests have been conducted to span the parameter space and to determine the confinement effect on both the rotor performance and the wake structure. The comparison demonstrated reasonable agreement with actuator-disk results, providing some validation of the present methodology, but underlining some of the limits of the existing theory. Thrust and power coefficients are increased by the blockage effect and it was found that the concept of equivalent free-stream velocity is beneficial to correct such parameters, although the traditional theory provides a slight overestimation of U'_{∞} compared to the present model. For highly loaded wind turbines, it is observed that the power coefficient can have already exceeded the Betz limit for $\epsilon \geqslant 0.02$, which is much smaller than the rule of thumb used in experimental practice which assumes that blockage effects are negligible for $\epsilon < 0.1$ (Wilson 1994).

Several aspects of the wake structure, like the wake radius and the wake pitch evolution (and their asymptotic states) have been discussed and it was found that the wake radius is reasonably well estimated by the actuator-disk approximation, but the pitch is not and an empirical correction scheme has been proposed here based on the available simulations. It is worth noting that the wake structure achieves its asymptotic state more quickly in the confined condition than in the unconfined one, probably due to the attenuation of radial motions imparted by the wall presence, an effect that can also have dynamical implications as it might attenuate the paring process of tip vortices.

Acknowledgements

This work was supported by the Swedish strategic research program STandUP for Energy. The authors wish to thank Professors H. Alfredsson and F. Bark and Dr R. Mikkelsen for fruitful discussions.

REFERENCES

BAHAJ, A. S., MOLLAND, A. F., CHAPLIN, J. R. & BATTEN, W. M. J. 2007 Power and thrust measurements of marine current turbines under various hydrodynamic flow conditions in a cavitation tunnel and a towing tank. *Renew. Energy* **32**, 407–426.

BARLOW, J. B., RAE, W. H. & POPE, A. 1999 *Low-Speed Wind Tunnel Testing*, 3rd edn. John Wiley & Sons.

BATCHELOR, G. K. 1967 *An Introduction to Fluid Dynamics*. Cambridge University Press.

BURTON, T., SHARPE, D., JENKINS, N. & BOSSANYI, E. 2001 *Wind Energy Handbook*. John Wiley & Sons.

CALLEGARI, A. J. & TING, L. 1978 Motion of a curved vortex filament with decaying vortical core and axial velocity. *J. Appl. Maths* **35**, 148–175.

CHEN, T. Y. & LIOU, L. R. 2011 Blockage corrections in wind tunnel tests of small horizontal-axis wind turbines. *Exp. Therm. Fluid Sci.* **35**, 565–569.

FUKUMOTO, Y. & MIYAZAKI, T. 1991 Three-dimensional distortions of a vortex filament with axial velocity. *J. Fluid Mech.* **222**, 369–416.

GARRETT, C. & CUMMINS, P. 2007 The efficiency of a turbine in a tidal channel. *J. Fluid Mech.* **588**, 243–251.

GLAUERT, H. 1935 Airplane propellers. In *Division L in Aerodynamic Theory* (ed. W. F. Durand), vol. 4, pp. 169–360. Springer.

GOODMAN, T. R. 1956 The tip correction for wind-tunnel tests of propellers. *J. Aeronaut. Sci.* **23**, 1094–1098.

JOUKOWSKY, N. E. 1912 Vortex theory of screw propeller. I. *Trudy Otdeleniya Fizicheskikh Nauk Obshchestva Lubitelei Estestvoznaniya* **16** (1), 1–31 (in Russian). French translation in *Théorie Tourbillonnaire de l'Hélice Propulsive*, pp. 1–47. Gauthier-Villars, 1929.

KATZ, J. & PLOTKIN, A. 1991 *Low-Speed Aerodynamics: From Wing Theory to Panel Methods*. McGraw-Hill.

KUIBIN, P. A. & OKULOV, V. L. 1998 Self-induced motion and asymptotic expansion of the velocity field in the vicinity of a helical vortex filament. *Phys. Fluids* **10**, 607–614.

LEISHMAN, J. G. 2000 *Principles of Helicopter Aerodynamics*. Cambridge University Press.

MCTAVISH, S., FESZTY, D. & NITZSCHE, F. 2013 An experimental and computational assessment of blockage effects on wind turbine wake development. *Wind Energy* doi:10.1002/we.1648.

MEDICI, D., IVANELL, S., DAHLBERG, J.-Å. & ALFREDSSON, P. H. 2011 The upstream flow of a wind turbine: blockage effect. *Wind Energy* **14**, 691–697.

MIKKELSEN, R. & SØRENSEN, J. N. 2002 Modeling of wind tunnel blockage. *Proceedings of the 2002 Global Windpower Conference and Exhibit*. European Wind Energy Association.

OKULOV, V. L. & SØRENSEN, J. N. 2010 Maximum efficiency of wind turbine rotors using Joukowsky and Betz approaches. *J. Fluid Mech.* **649**, 497–508.

RICCA, R. L. 1994 The effect of torsion on the motion of a helical vortex filament. *J. Fluid Mech.* **273**, 241–259.

SEGALINI, A. & ALFREDSSON, P. H. 2013 A simplified vortex model of propeller and wind-turbine wakes. *J. Fluid Mech.* **725**, 91–116.

SØRENSEN, J. N. & SHEN, W. Z. 2002 Numerical modelling of wind turbine wakes. *Trans. ASME: J. Fluids Engng* **124**, 393–399.

TROLDBORG, N. 2008 Actuator line modeling of wind turbine wakes. PhD thesis, Technical University of Denmark.

VERMEER, L. J., SØRENSEN, J. N. & CRESPO, A. 2003 Wind turbine wake aerodynamics. *Prog. Aerosp. Sci.* **39**, 467–510.

WERLE, M. J. 2010 Wind turbine wall-blockage performance corrections. *J. Propul. Power* **26**, 1317–1321.

WILSON, R. E. 1994 Aerodynamic behavior of wind turbines. In *Wind Turbine Technology, Fundamental Concepts of Wind Turbine Engineering* (ed. D. Spera), pp. 215–282. ASME Press.